Event-Based Multi-Range Radiance Separation and 3D Reconstruction via Line-Scan Pseudo-Square Illumination

Ryuji Hashimoto[1] Yuta Asano[2] Shin Ishihara[2] Bohan Yu[3] Chu Zhou[2]
Boxin Shi[3] Imari Sato[1,2]

[1]The University of Tokyo [2]National Institute of Informatics [3]Peking University

ryuji1352@g.ecc.u-tokyo.ac.jp, {asanoy, sishihara, imarik}@nii.ac.jp,
zhou_chu@hotmail.com, {ybh1998, shiboxin}@pku.edu.cn

Abstract

Decomposing scene radiance into physically meaningful components, including direct reflection, interreflection, and scattering, enables a deeper understanding of scene appearance. In this paper, we propose the first method to perform multi-range radiance component separation using only events captured by an event camera, without requiring any additional frame-based measurements. Our approach scans the scene by swiping line-shaped illumination across it, while exploiting the event camera's high temporal resolution and wide dynamic range to recover both direct and multiple global components corresponding to different light propagation distances. To address the noise inherent in event-integration-based radiance recovery, we present a pixel-wise calibration strategy that leverages the reproducibility of per-pixel noise patterns. We demonstrate that this calibration is highly effective in suppressing noise, enabling stable recovery from subtle signals. Moreover, we show that by detecting the timing at which the scanning line passes each pixel, the same line-scan event data can be exploited for coarse 3D reconstruction. Experimental results on real scenes show that our event-based approach achieves faster and finer component separation, while also enabling coarse depth estimation without the exposure control required by frame-based cameras.

1. Introduction

Physics-based models have long played a crucial role in computer vision, as they provide principled formulations that allow problems to be solved in accordance with physical reflectance properties. Within this framework, separating scene radiance into direct and global components is a fundamental task, since it yields a cleaner representation of appearance that corresponds to the visual phenomena targeted by physics-based modeling. In particular, isolating the direct component, corresponding to light that reaches the camera after a single surface reflection, directly supports the assumptions of such models and can significantly enhance the accuracy and applicability of the vision approaches built upon them, such as photometric stereo [14] and structured light 3D reconstruction [18]. In contrast, the global component, which arises from interreflection, scattering, and subsurface light transport, encodes valuable information about material properties, supporting applications such as material classification [9] and scene editing [14].

A pioneering work by Nayar *et al*. [14] introduced the separation of direct and global components using a projector–camera system, which laid the groundwork for many subsequent studies in this field. Wu *et al*. [29] used an ultrafast time-of-flight (ToF) imaging system to distinguish between interreflection and subsurface scattering, both included in global component. Other approaches attempt to decompose the global components into near- and far-range components based on light propagation distance [9, 17, 19, 20]. The ring light imaging method [16] was introduced to capture transient subsurface scattering by illuminating each surface point to form ring-shaped light patterns with increasing radii. By analyzing the images corresponding to each ring radius, this approach enables the estimation of path-length-dependent subsurface light transport using a conventional camera. However, it requires point-by-point scanning, leading to long acquisition times and its use in practical applications remains challenging.

This paper presents the first effective event-camera-based method that relies solely on event-camera signals to separate direct and multiple global radiance components, ranging from near to far. Event cameras are now widely utilized in various tasks of computer vision such as 3D reconstruction [4, 8, 12, 31], photometric stereo [32], and hyperspectral imaging [33], since they can offer high temporal resolution and a broad dynamic range with small data size.

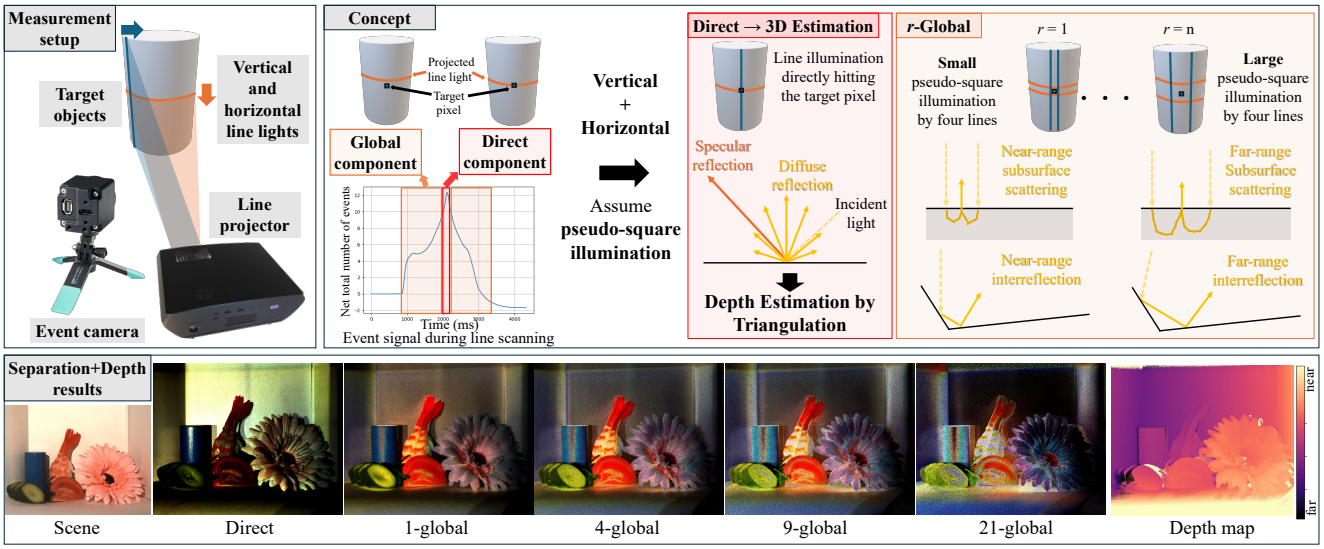

Figure 1. Overview of the proposed event-camera method. The scene is scanned with vertical and horizontal line illuminations to approximate pseudo-square patterns at varying distances r. The event camera records temporal radiance changes to separate direct and multi-range global components. The same data are also used for coarse 3D reconstruction via scan-line timing.

These properties are also useful for direct-global separation. Zhou *et al*. [34] combined the frame-based camera with the event camera and achieved real-time acquisition of the direct and global components. While this method facilitates rapid acquisition, it remains confined to two-component separation and necessitates a training phase as part of the process.

In contrast, our method separates finely into direct and multiple global radiance components, ranging from near to far range, only using an event camera. Our method scans the scene by swiping line-shaped illumination while the event camera records fine-grained temporal brightness changes as the illumination moves relative to the observation point. By leveraging the event camera's high temporal resolution and wide dynamic range, our method enables multi-range light transport decomposition. We also propose a noise mitigation strategy for integration-based radiance recovery exploiting the reproducibility of pixel-wise noise patterns, which significantly reduce the noise. Since the fine component separation relies on subtle differences in the event signal, this strategy is fundamental to our method. Moreover, the same event data used for radiance separation enables coarse 3D reconstruction by exploiting the timing information when the scanning line passes each pixel. We demonstrate that our approach achieves coarse 3D reconstruction, along with finer separation with significantly less data, which is hard to accomplish at the same time with a conventional frame-based camera.

To summarize, our contributions are as follows:

- We propose an efficient way for capturing approximate multi-range light transport components separated due to light propagation distance using line scanning illumination patterns.
- We implemented the approximate separation method on an event camera for faster and finer acquisition with less data compared to frame-based implementation.
- Using the same data as for the radiance component separation, we also reconstruct the 3D shape of scene.
- We propose a noise mitigation method suitable for our line scanning based separation.

2. Related Works

2.1. Radiance Component Separation

Direct-Global Component Separation. Direct-global component separation divides scene radiance into exactly two components: the direct component and the global component. A pioneering method by Nayar *et al*. [14] employs high-frequency illumination with complementary patterns for radiance separation. While in theory only two complementary patterns are sufficient, in practice 6–8 patterns (or more for complex scenes) are typically required to achieve stable and reliable results. Afterwards, many methods have been proposed to improve it in various directions. Gu *et al*. [6] reduced the number of required images and improved SNR by using multiple light sources. Motion compensation is employed [1] to enable direct-global separation in dynamic scenes. The separation at high frame rates has been achieved using the combination of high-speed camera with temporal dithering of DLP projector [13], and hybrid RGB–event cameras with sweeping line occluders [34]. Some methods exploited image priors [5, 15, 25] to achieve

single-frame separation.

Finer Component Decomposition. Finer decomposition aims to split radiance into multiple detailed components rather than only direct and global. Lamond *et al*. [10] separated the direct component into diffuse and specular terms by exploiting differences in their dependency on light incident direction. The global component can be further decomposed into the interreflection and the subsurface scattering components by using the time of flight (ToF) imaging device [29] or applying independent vector analysis to different direct components acquired under multiple frequency illumination [24]. Near- and far-range global components can be distinguished based on light propagation distance using sinusoidal patterns [20], primal–dual imaging [17, 19], or synchronized projector–camera setups [9]. Seitz *et al*. [22] decomposed the radiance by interreflection into multiple components that are contributed by specific number of light bounces in the scene. Tanaka *et al*. [27] modeled the appearance of translucent object using depth-dependent point spread function and recovered inner slices of them by exploiting multiple frequency checkerboard illumination patterns.

Most prior finer decomposition methods [9, 17, 19, 20] split the global component into only two categories: near- and far-range. In contrast, our approach decomposes it into multiple finer components corresponding to different light propagation distances. While ring-light imaging [16] can also achieve such fine separation, it is impractically slow due to the need for capturing images under point-by-point illumination on each surface point. We address this by combining an event camera with line-scanning illumination, greatly reducing acquisition time.

2.2. Event-Based Active Lighting

Event cameras record per-pixel brightness changes asynchronously when the logarithmic irradiance exceeds a threshold, offering high dynamic range, fine temporal resolution, and compact data storage. These properties make them well-suited for active lighting applications across a variety of tasks.

Direct-Global Component Separation. Zhou *et al*. [34] introduced an event-guided system to separate the direct and global components, which enables real-time acquisition. First, scene radiance is captured by an RGB frame-based camera. Then using an event camera, they capture the change in direct and global components when line occluder is swept over the light source. The captured image and the event data are then fused using neural network to form RGB results of direct and global image.

Although our approach doesn't support real-time acquisition, ours has three advantages over theirs. First, their method can only separate into direct and global components, while ours can further separate the global component into multiple components. Second, our method only utilizes the event camera, in other words, the frame-based camera is not required. Third, they need to collect dataset for learning on the neural network, while ours doesn't have to.

Geometry Estimation. EventPS [32] used a high-speed rotating light source to perform real-time photometric stereo from continuous lighting changes. For depth sensing, structured-light systems combining an event camera with a laser-point projector [12] or digital light projector [8] have been proposed. To reduce the effect of global components on reconstruction accuracy, epipolar constraints have been applied in software [4, 31]. Liu *et al*. [11] combined an event camera with a flying-spot projector, and the dual photography technique [23] to reconstruct 3D shape of transparent objects in both line-of-sight and non-line-of-sight scenes.

Other Applications. Takatani *et al*. [26] proposed bispectral difference imaging using temporally modulated illumination. Chen *et al*. [2] developed a practical indoor localization system with multiple LEDs and event-based Gaussian mixture tracking. Han *et al*. [7] introduced transient event frequency for precise radiance recovery from high-temporal-resolution event signals under active illumination.

3. Proposed Method

This section describes our method for separating radiance components according to light propagation distance and performing coarse 3D reconstruction. These are both performed using the same measurements by an event camera that records the radiance change during line illumination sweeping over the scene. In Section 3.1, we first define the direct and r-global components and introduce a practical approximation based on line-scanning illumination. We then explain how these components can be recovered from event-camera data in Section 3.2, and describe how timing information in the same data enables coarse 3D reconstruction in Section 3.3. Finally, a denoising strategy crucial to recovery of fine components separation is described in Section 3.4.

3.1. Multi-Range Radiance Separation

3.1.1 Definitions of Direct and r-Global Components

When light is incident on a point on a surface, it may exit near the incident point or reappear at a distant location after undergoing subsurface scattering or interreflection (Figure 1). Previous studies [9, 17, 19, 20] have demonstrated that analyzing the distance between the incident and exit points allows the separation of direct and near-/far-range global components. To enable finer decomposition of light transport, the radiance observed at the center of a ring-shaped illumination pattern can be used [16]. We derive a practical approach to estimate the radiance.

Let us first consider how the distance between the incident point and the observation point affects the appearance. When only the surface point corresponding to pixel (i, j) is illuminated, the radiance at (x, y) is given by $I(x, y) = T(i, j, x, y)$, where T is a light transport function of the scene, representing how much light incident at the surface point corresponding to (i, j) transmits to the camera pixel (x, y).

When all scene points are illuminated, the radiance at (x, y) can be expressed as the sum of the direct component and the global component propagated from ring-shaped regions at different radii:

$$\begin{aligned} I_{\text{all}}(x, y) &= \sum_{(i,j)} T(i, j, x, y) \\ &= T(x, y, x, y) + \sum_{r>0} \sum_{(i,j)\in D_r} T(i, j, x, y), \quad (1) \\ D_r :&\{(i, j)|(i - x)^2 + (j - y)^2 = r\}, \end{aligned}$$

where D_r denotes the set of camera pixels forming a ring of radius r centered at (x, y). The first term $T(x, y, x, y)$ represents the direct component I_d resulting from incident light at the same location (x, y), while the second term represents the global component I_g, arising from indirect illumination with ring-shaped patterns of varying radii $(r > 0)$, as examined in [16].

Here, we define r-global component I_{g_r} for each distance r as:

$$I_{g_r}(x, y) = \sum_{(i,j)\in D_r} T(i, j, x, y). \quad (2)$$

Our goal is to recover both the direct component I_d and the r-global component I_{g_r} for different radius r.

3.1.2 Line-Scan Approximation

Accurate computation of I_d and I_{g_r} is possible by fully measuring the light transport T, e.g., via impulse illumination scanning. However, this requires as many measurements as the number of pixels $(H \times W)$, where low per-pixel radiance demands long exposures, and separating multi-range global components needs even longer acquisition to capture subtle variations.

Instead of impulse illumination, we use horizontal and vertical line illuminations to sweep over the scene, reducing the required measurements from $H \times W$ to $H + W$. We approximate I_d and I_{g_r} as the sum of the international components generated by four-line illuminations positioned at a certain distance in both horizontal and vertical directions: left, right, top, and bottom. To achieve further efficient measurement, we use an event camera which has high dynamic range property and thus can detect fine variation without long exposure.

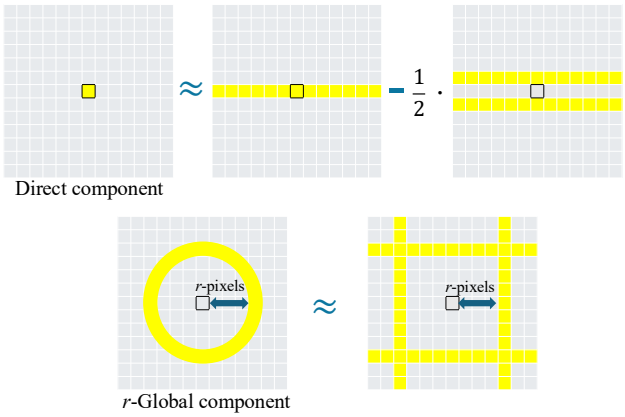

Figure 2. Approximation of the direct (above) and r-global (below) components using line scanning. The direct component is approximated with the difference of radiance when the line is projected exactly on the pixel and the line is on adjacent pixels. The r-global component is approximated with four lines r pixels apart from the center.

Let I_j^{hor} denote the radiance observed when illuminating the j-th row (horizontal line):

$$I_j^{\text{hor}}(x, y) = \sum_{i=1}^{W} T(i, j, x, y). \quad (3)$$

Similarly, I_i^{ver} is the radiance when illuminating the i-th column (vertical line).

Previous studies separate direct and global components by assuming that the global component varies smoothly across space. Likewise, in our scanned-line illumination case, we assume that the global component under a given line illumination changes smoothly, remaining similar when the line position is slightly shifted. Thus, as illustrated in Figure 2, the direct component at (x, y) can be approximated as:

$$I_d \approx I_y^{\text{hor}} - \frac{1}{2}(I_{y-1}^{\text{hor}} + I_{y+1}^{\text{hor}}), \quad (4)$$

where we omit (x, y) for brevity.

Similarly, the r-global component can be obtained by combining the vertical and horizontal contributions of the square light in Figure 2.

$$I_{g_r} \approx I_{y-r}^{\text{hor}} + I_{y+r}^{\text{hor}} + I_{x-r}^{\text{ver}} + I_{x+r}^{\text{ver}}. \quad (5)$$

To confirm the validity of this approximation, we compare the radiance under three illumination types—(1) ring-shaped, (2) square-shaped, and (3) our pseudo-square illumination from four lines across four materials: paper, rubber, soap, and sponge (Figure 3). For more translucent materials such as soap and sponge, stronger near-range global components (i.e., for small radius r) are observed under pseudo-square illumination, due to the influence of

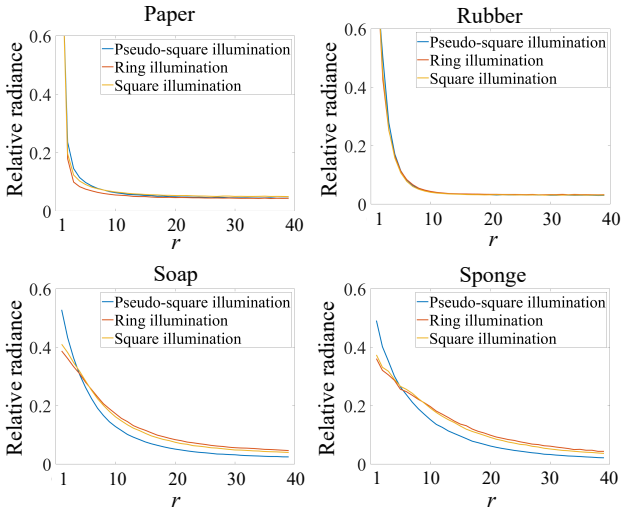

Figure 3. Comparison of radiance at specific point of four materials under ring-shaped illumination, square-shaped illumination, and our proposed pseudo-square illumination formed by four line illuminations at each distance from the point.

line light located outside the pseudo-square region. However, for larger r, the relative radiance takes similar decline patterns. In contrast, for more opaque materials such as paper and rubber, the r-global components are nearly identical across all three illumination conditions, regardless of radius.

3.2. Event-Based Radiance Recovery under Line Illumination

Each event camera pixel triggers when the change in logarithmic radiance exceeds a contrast threshold: θ^+ for positive (brightening) changes and θ^- for negative (darkening) changes. An event is then represented as (x, y, p, t), where (x, y) is the pixel, p is the polarity (1 for brightening, 0 for darkening), and t is the timestamp. In summary, the event signal at pixel (x, y) at time t is given by:

$$\begin{cases} (x, y, 1, t) & \text{if } \log I_e(x, y, t) \\ & \quad \geq \log I_e(x, y, t_{\text{prev}}) + \theta^+ \\ (x, y, 0, t) & \text{if } \log I_e(x, y, t) \\ & \quad \leq \log I_e(x, y, t_{\text{prev}}) - \theta^- \\ \text{no events} & \text{otherwise,} \end{cases} \tag{6}$$

where $I_e(x, y, t)$ represents the radiance at pixel (x, y) at time t, and t_{prev} denotes the timestamp when the previous event occurred.

Relative radiance value at time t can be calculated by integrating multiple events and exponentiating the relation in (6) [3, 7]:

$$N(x, y, t) = n^+(x, y, t)\theta^+ - n^-(x, y, t)\theta^- \tag{7}$$

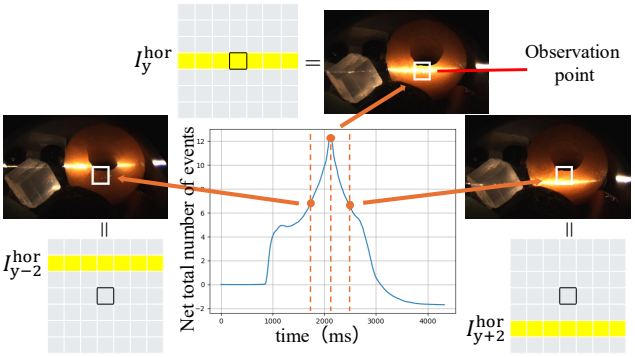

Figure 4. The radiance when the line is projected exactly on the pixel is recovered from the peak of the net total number of events, while the radiance when the line is on desired distance is recovered from the net number of events at the time point with corresponding time difference.

$$\frac{I_e(x, y, t)}{I_e(x, y, t_0)} = \exp(N(x, y, t)), \tag{8}$$

where t_0 is the timestamp at which the recording begins, n^+ and n^- represent the total number of positive and negative events, respectively, and N is the net total number of events that occurred at pixel (x, y) from t_0 to t. Following the approach in [3, 7], we set $I_e(x, y, t_0) = 1$ by initiating the recording in a dark environment, thereby enabling recovery of the radiance value $I_e(x, y, t)$ with respect to the brightness in the environment.

Next, we show how to recover $I^{\text{hor}}_{y\pm r}(x, y)$ for each r from the event data captured during horizontal line scanning illumination. The scanning speed v of the line illumination (in pixels per second) is assumed to be pre-measured. First, we detect the peak from the radiance transition at (x, y) to determine the time when the line passes over row y (Figure 4):

$$t_{\text{peak}} = \underset{t}{\text{argmax}}\ N(x, y, t). \tag{9}$$

Then, $I^{\text{hor}}_{y\pm r}$ in Equations (4) and (5) can be obtained from the recovered radiance at a time offset by r pixels:

$$I^{\text{hor}}_{y\pm r}(x, y) = I_e(x, y, t_{\text{peak}} \pm r/v). \tag{10}$$

Similarly, $I^{\text{ver}}_{x\pm r}$ is recovered from vertical scanning data.

This enables the recovery of $I^{\text{hor}}_{y\pm r}$ and $I^{\text{ver}}_{x\pm r}$ for all r using a single scan for horizontal and vertical line illuminations, respectively. Since this method is applied uniformly across all camera pixels, images of the direct component and the r-global component can then be computed from Equations (4) and (5).

3.3. 3D Reconstruction

t_{peak} obtained from Equation (9) can be used to obtain a coarse 3D geometry of the scene. As illustrated in Figure 5,

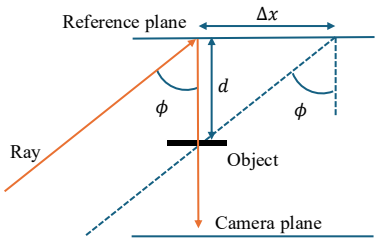

Figure 5. Geometric relationship between the camera, reference plane, and light rays for our coarse 3D reconstruction. We assume that the light rays incident to the camera plane are perpendicular to the plane, and the angles between the light rays and the normal of the reference plane are constant across the scene.

we define a reference plane parallel to the camera plane and recover the distance d from this plane to each object point. For simplicity, we make the following two assumptions: (1) The distance from the objects to the camera plane is sufficiently large. (2) The light source produces rays at a constant angle ϕ with respect to the normal of the reference plane, and the scanning speed v of the projected line is constant. From assumption (1), all light rays entering the camera can be considered perpendicular to the camera plane. Under these conditions, triangulation geometry yields:

$$d = \frac{\Delta x}{\tan\phi} = \frac{v}{\tan\phi}\Delta t, \tag{11}$$

where Δx is the displacement of the illumination line between the reference plane and the object surface, and Δt is the corresponding time difference. Since both v and ϕ are constant, $d \propto \Delta t$, meaning that relative depth can be estimated by measuring Δt.

To compute Δt, we first measure $t^{\text{ref}}_{\text{peak}}$ using a flat reference plane. Subtracting this from t_{peak} measured on the actual scene gives: $\Delta t = t_{\text{peak}} - t^{\text{ref}}_{\text{peak}}$.

3.4. Pixel-Wise Denoising using Reproducible Noise

Radiance recovery by event integration often exhibits significant noise, due to inter-pixel variation in the contrast thresholds [7, 28, 30]. We observed that this noise pattern is highly reproducible across different recordings under line scanning illumination patterns (Figure 6).

To mitigate this noise, we employed an approach similar to the flat-field correction [21] used in [30], but adopted it specifically for our line scanning approach. Since positive events dominate before t_{peak} and negative events dominate after, we treat these intervals separately. First, for $t \le t_{\text{peak}}$, the deviation ratio is calculated as

$$\rho_{\text{before}}(x,y) = \frac{N^{\text{ref}}(x,y,t_{\text{peak}})}{\bar{N}^{\text{ref}}(t_{\text{peak}})}, \tag{12}$$

where N^{ref} represents the net total number of events of each pixel from white-target scanning, and $\bar{N}^{\text{ref}}$ represents its average. Then, we correct the recovered radiance on scene as $\hat{I}^{\text{scene}}_e(x,y,t) = \exp(N^{\text{scene}}(x,y,t)/\rho_{\text{before}}(x,y))$. For $t > t_{\text{peak}}$, both pre- and post-t_{peak} deviations contribute, so calculate the deviation ratio as

$$\rho_{\text{after}}(x,y) = \frac{N^{\text{ref}}(x,y,t_{\text{after}}) - N^{\text{ref}}(x,y,t_{\text{peak}})}{\bar{N}^{\text{ref}}(t_{\text{after}}) - \bar{N}^{\text{ref}}(t_{\text{peak}})}, \tag{13}$$

where t_{after} is a sufficiently later time than t_{peak}.

The final calibrated radiance is:

$$\hat{I}^{\text{scene}}_e(x,y,t) = \exp\{\frac{N^{\text{scene}}(x,y,t_{\text{peak}})}{\rho_{\text{before}}(x,y)} + \frac{N^{\text{scene}}(x,y,t_{\text{after}}) - N^{\text{scene}}(x,y,t_{\text{peak}})}{\rho_{\text{after}}(x,y)}\}. \tag{14}$$

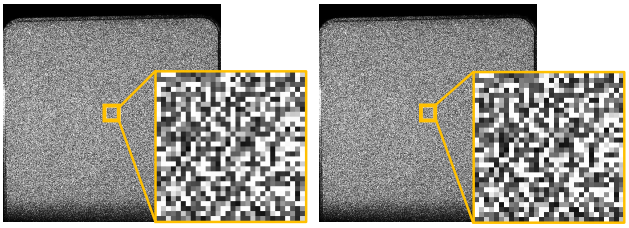

Figure 6. Radiance recovery results without denoising from line scanning on a white target. Although the images in the left and right columns come from different recordings, they exhibit very similar noise patterns.

4. Experimental Results

We constructed measurement systems for an event-based camera and performed the fine radiance component separation and 3D reconstruction in real scenes containing diverse light transport effects. For clarity of discussion, the distance r was defined in pixel units in Section 3. In practice, however, aligning the pixel units of the projector and camera is challenging. Therefore, in the real-scene experiments, r was defined with respect to the line thickness. To obtain reference results for the separation, we also implemented same setting with a frame-based camera.

4.1. Experimental Setup and Conditions

Figure 7 shows our experimental setup, and Table 1 lists the components. Line illuminations are generated by a DLP projector and positioned by motorized stages.

For the frame camera (FLIR GS3-U3-23S6C-C), the scan speed was set so that the line moved at most one pixel between frames, resulting in about 60 s for two scans. For the event camera, the scan speed was limited to avoid event-rate saturation, yielding about 20 s for two scans. Event-camera data sizes were much smaller than frame-camera

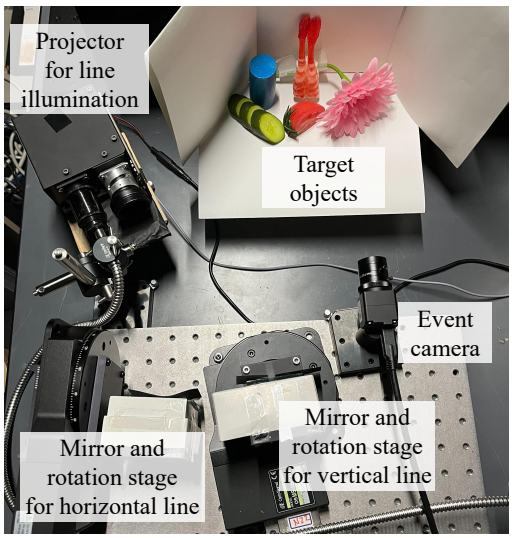

Figure 7. Our imaging setup. A projector emits a line of light, which is reflected by mirrors rotating horizontally and vertically. The moving reflected line is then captured by the event camera.

ones. For example, for the flower-in-glass scene in Figure 10, the event-camera recording was about 500 MB, while the frame-camera data was about 20 GB.

Equipment	Manufacturer	Model
Event camera	CenturyArks	SilkyEvCam HD
Light source	Asahi Spectra	MAX-S310
DLP projector	Digital Light Innovations	CEL5500-Fiber
Rotation stage	OptoSigma	OSMS-120YAW
Stage controller	OptoSigma	HSC-103

Table 1. Details of the equipment for the experimental setup.

4.2. Pixel-Wise Denoising for Radiance Recovery

We applied the proposed pixel-wise calibration method (Section 3.4) to mitigate integration noise. As shown in Figure 8, this calibration significantly reduces noise and makes the difference in brightness among patches more apparent. The decrease in the coefficient of variation was approximately 61% on average (Table 2).

Patch	1	2	3	4	5	6
Before denoise	0.36	0.39	0.45	0.58	0.78	1.47
After denoise	0.06	0.10	0.18	0.24	0.28	1.11

Table 2. Coefficient of variation in bottom 6 patches (white to black) of color checker in Figure 8. The proposed denoising method significantly reduces the coefficient of variation.

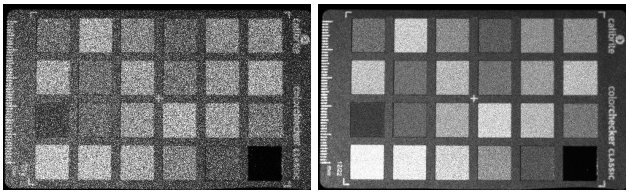

Before denoising After denoising

Figure 8. Radiance recovery results on a color checker chart before and after the proposed pixel-wise denoising. The raw integration of events (left) suffers from strong pixel-wise noise patterns, while the calibrated recovery (right) significantly reduces noise, revealing clean intensity levels across patches.

4.3. Radiance Separation and Depth Estimation on Real Scenes

We present both monochrome results for scenes with low chromatic variation and RGB results for high-color variation scene. RGB results were captured using the same high-resolution monochrome event camera by sequentially projecting red, green, and blue line illuminations and combining the recovered channels. In RGB measurements, a band-pass filter reduced illumination intensity, producing fewer events and fewer separable components.

Figure 9 shows monochrome results from the frame and event cameras. In the carved bone scene, a carved bone with a hollow interior causes multi-scale interreflections: the 1-global component captures interreflections along outer-surface pattern edges, while far-range globals reveal light entering the interior, particularly in event-based results. In the rice ball scene, the direct component shows surface specularities, the 1-global component is dominated by sub-surface scattering within grains, and far-range globals capture interreflections and scattering between grains.

Figure 10 shows RGB results. In the Anmitsu scene, both methods capture surface colors in the direct component and interreflections in globals, but event-based results more clearly show the spatial shift of bright interreflection regions as r increases. In the flowers-in-glass scene, petal globals indicate interreflections, and the glass remains bright in far-range globals due to refraction.

Overall, with the proposed denoising method, the event-camera results achieve direct components with noise levels comparable to those of the frame-based results, while the high dynamic range of the event camera allows for clearer capture of far-range global components.

Regarding the results of the coarse 3D reconstruction, all of them appear to be roughly plausible including subsurface scattering areas such as the apricot in Anmitsu. However, in transparent areas such as the glass bowl, reconstruction failed due to peak estimation error caused by refraction.

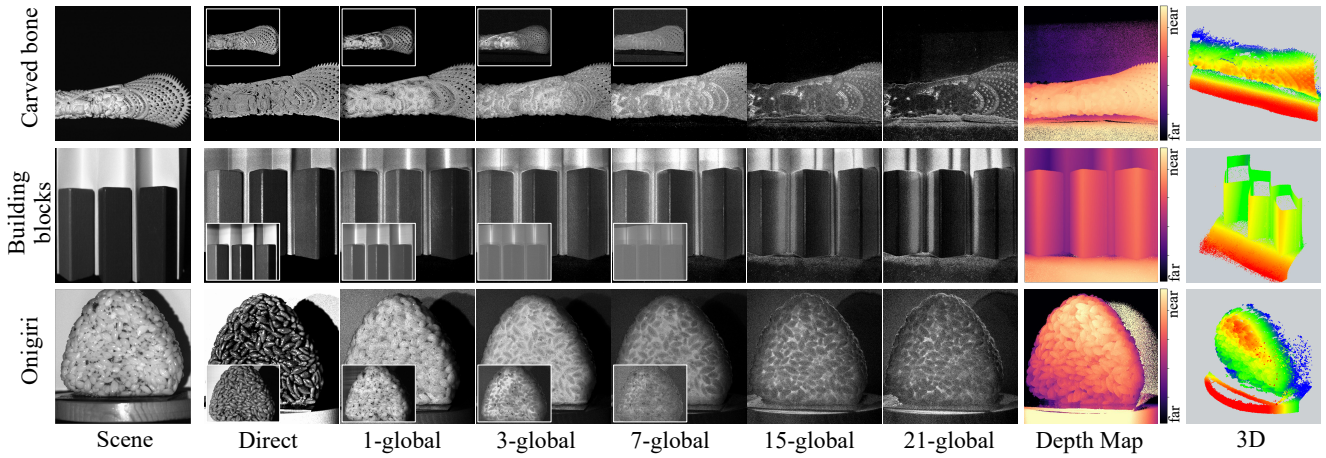

Figure 9. Monochrome separation results on real scenes: Carved bone, Building blocks, and Onigiri. For each scene, the direct component and multiple r-global components are reconstructed from event-camera data, along with the estimated depth map and coarse 3D reconstruction. **White-bordered images are reference results** obtained by applying the proposed separation method to data captured with a conventional frame camera. Due to the limited dynamic range of the frame camera, meaningful separation results beyond 7-global could not be reliably recovered and are therefore not reported. Note that the brightness of each component has been adjusted for visualization.

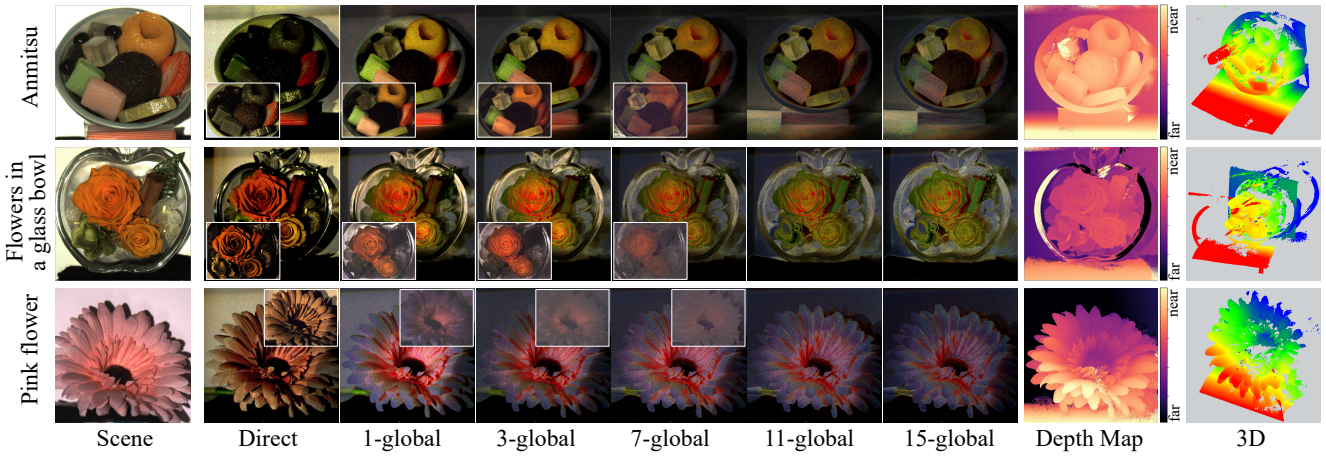

Figure 10. RGB separation results on real scenes: Anmitsu, Flowers in a glass bowl, and Pink flower. As in the monochrome results, white-bordered images are reference results obtained from frame-camera data, which are shown only up to 7-global due to the limited dynamic range of the frame camera. Note that the brightness of each component has been adjusted for visualization.

5. Conclusion

We proposed an event-camera framework for multi-range radiance component separation using line-shaped illumination. It recovers direct and multiple global components, mitigates integration noise via pixel-wise calibration, and enables coarse 3D reconstruction from the same data. Experiments show that our approach achieves finer separation than frame-based methods, with shorter acquisition time and smaller data size.

Limitations and Future Works. Although our event-based approach significantly reduces acquisition time, it is still not fast enough for dynamic scenes. Future work includes addressing event-rate saturation at high scan speeds, potentially via learning-based radiance recovery to complement missing events. Additionally, the current 3D reconstruction is limited to coarse geometry due to simplifying assumptions. Careful calibration of the event camera and light source could enable more precise metric reconstruction.

Acknowledgments

This work is supported by JST-Mirai Program under Grant No. JPMJM123G1, and JSPS Kakenhi under Grant No. 20H05953, 25K21236, 23K16911.

References

[1] Supreeth Achar, Stephen T. Nuske, and Srinivasa G. Narasimhan. Compensating for motion during direct-global separation. In *2013 IEEE International Conference on Computer Vision*, pages 1481–1488, 2013. 2

[2] Guang Chen, Wenkai Chen, Qianyi Yang, Zhongcong Xu, Longyu Yang, Jörg Conradt, and Alois Knoll. A novel visible light positioning system with event-based neuromorphic vision sensor. *IEEE Sensors Journal*, 20(17):10211–10219, 2020. 3

[3] Zehao Chen, Qian Zheng, Peisong Niu, Huajin Tang, and Gang Pan. Indoor lighting estimation using an event camera. In *2021 IEEE/CVF Conference on Computer Vision and Pattern Recognition (CVPR)*, pages 14755–14765, 2021. 5

[4] Aniket Dashpute, Jiazhang Wang, James Taylor, Oliver Cossairt, Ashok Veeraraghavan, and Florian Willomitzer. Event-based motion-robust accurate shape estimation for mixed reflectance scenes. *arXiv preprint arXiv:2311.09652*, 2023. 1, 3

[5] Zhaoliang Duan, James Bieron, and Pieter Peers. Deep separation of direct and global components from a single photograph under structured lighting. In *Computer Graphics Forum*, pages 459–470. Wiley Online Library, 2020. 2

[6] Jinwei Gu, Toshihiro Kobayashi, Mohit Gupta, and Shree K. Nayar. Multiplexed illumination for scene recovery in the presence of global illumination. In *2011 International Conference on Computer Vision*, pages 691–698, 2011. 2

[7] Jin Han, Yuta Asano, Boxin Shi, Yinqiang Zheng, and Imari Sato. High-fidelity event-radiance recovery via transient event frequency. In *Proceedings of the IEEE/CVF Conference on Computer Vision and Pattern Recognition (CVPR)*, pages 20616–20625, 2023. 3, 5, 6

[8] Xueyan Huang, Yueyi Zhang, and Zhiwei Xiong. High-speed structured light based 3d scanning using an event camera. *Optics Express*, 29(22):35864–35876, 2021. 1, 3

[9] Hiroyuki Kubo, Suren Jayasuriya, Takafumi Iwaguchi, Takuya Funatomi, Yasuhiro Mukaigawa, and Srinivasa G Narasimhan. Programmable non-epipolar indirect light transport: Capture and analysis. *IEEE Transactions on Visualization and Computer Graphics*, 27(4):2421–2436, 2019. 1, 3

[10] Bruce Lamond, Pieter Peers, and Paul E Debevec. Fast image-based separation of diffuse and specular reflections. *SIGGRAPH Sketches*, 6, 2007. 3

[11] Xiaomeng Liu, Joshua D. Rego, Suren Jayasuriya, and Sanjeev J. Koppal. Event-based dual photography for transparent scene reconstruction. *Opt. Lett.*, 48(5):1304–1307, 2023. 3

[12] Manasi Muglikar, Guillermo Gallego, and Davide Scaramuzza. Esl: Event-based structured light. In *2021 International Conference on 3D Vision (3DV)*, pages 1165–1174. IEEE, 2021. 1, 3

[13] Srinivasa G Narasimhan, Sanjeev J Koppal, and Shuntaro Yamazaki. Temporal dithering of illumination for fast active vision. In *European Conference on Computer Vision*, pages 830–844. Springer, 2008. 2

[14] Shree K Nayar, Gurunandan Krishnan, Michael D Grossberg, and Ramesh Raskar. Fast separation of direct and global components of a scene using high frequency illumination. In *ACM SIGGRAPH 2006 Papers*, pages 935–944. 2006. 1, 2

[15] Shijie Nie, Lin Gu, Art Subpa-Asa, Ilyes Kacher, Ko Nishino, and Imari Sato. A data-driven approach for direct and global component separation from a single image. In *Computer Vision–ACCV 2018: 14th Asian Conference on Computer Vision, Perth, Australia, December 2–6, 2018, Revised Selected Papers, Part VI 14*, pages 133–148. Springer, 2019. 2

[16] Ko Nishino, Art Subpa-Asa, Yuta Asano, Mihoko Shimano, and Imari Sato. Variable ring light imaging: capturing transient subsurface scattering with an ordinary camera. In *Proceedings of the European Conference on Computer Vision (ECCV)*, pages 598–613, 2018. 1, 3, 4

[17] Matthew O'Toole, Ramesh Raskar, and Kiriakos N Kutulakos. Primal-dual coding to probe light transport. *ACM Trans. Graph.*, 31(4):39–1, 2012. 1, 3

[18] Matthew O'Toole, John Mather, and Kiriakos N Kutulakos. 3d shape and indirect appearance by structured light transport. In *Proceedings of the IEEE Conference on Computer Vision and Pattern Recognition*, pages 3246–3253, 2014. 1

[19] Matthew O'Toole, Supreeth Achar, Srinivasa G Narasimhan, and Kiriakos N Kutulakos. Homogeneous codes for energy-efficient illumination and imaging. *ACM Transactions on Graphics (ToG)*, 34(4):1–13, 2015. 1, 3

[20] Dikpal Reddy, Ravi Ramamoorthi, and Brian Curless. Frequency-space decomposition and acquisition of light transport under spatially varying illumination. In *Computer Vision–ECCV 2012: 12th European Conference on Computer Vision, Florence, Italy, October 7-13, 2012, Proceedings, Part VI 12*, pages 596–610. Springer, 2012. 1, 3

[21] James Anthony Seibert, John M Boone, and Karen K Lindfors. Flat-field correction technique for digital detectors. In *Medical Imaging 1998: Physics of Medical Imaging*, pages 348–354. SPIE, 1998. 6

[22] S.M. Seitz, Y. Matsushita, and K.N. Kutulakos. A theory of inverse light transport. In *Tenth IEEE International Conference on Computer Vision (ICCV'05) Volume 1*, pages 1440–1447 Vol. 2, 2005. 3

[23] Pradeep Sen, Billy Chen, Gaurav Garg, Stephen R. Marschner, Mark Horowitz, Marc Levoy, and Hendrik P. A. Lensch. Dual photography. In *ACM SIGGRAPH 2005 Papers*, page 745–755, New York, NY, USA, 2005. Association for Computing Machinery. 3

[24] Art Subpa-Asa, Yinqiang Zheng, Nobutaka Ono, and Imari Sato. Light transport component decomposition using multi-frequency illumination. In *2017 IEEE International Conference on Image Processing (ICIP)*, pages 3595–3599. IEEE, 2017. 3

[25] Art Subpa-Asa, Ying Fu, Yinqiang Zheng, Toshiyuki Amano, and Imari Sato. Separating the direct and global components of a single image. *Journal of Information Processing*, 26:755–767, 2018. 2

[26] Tsuyoshi Takatani, Yuzuha Ito, Ayaka Ebisu, Yinqiang Zheng, and Takahito Aoto. Event-based bispectral photometry using temporally modulated illumination. In *Proceedings*

of the IEEE/CVF Conference on Computer Vision and Pattern Recognition, pages 15638–15647, 2021. 3

[27] Kenichiro Tanaka, Yasuhiro Mukaigawa, Hiroyuki Kubo, Yasuyuki Matsushita, and Yasushi Yagi. Recovering inner slices of layered translucent objects by multi-frequency illumination. *IEEE transactions on pattern analysis and machine intelligence*, 39(4):746–757, 2016. 3

[28] Ziwei Wang, Yonhon Ng, Pieter van Goor, and Robert Mahony. Event camera calibration of per-pixel biased contrast threshold. In *Australasian Conference of Robotics and Automation (ACRA)*, 2019. 6

[29] Di Wu, Andreas Velten, Matthew O'Toole, Belen Masia, Amit Agrawal, Qionghai Dai, and Ramesh Raskar. Decomposing global light transport using time of flight imaging. *International journal of computer vision*, 107:123–138, 2014. 1, 3

[30] Yuliang Wu, Ganchao Tan, Jinze Chen, Wei Zhai, Yang Cao, and Zheng-Jun Zha. Event-based asynchronous hdr imaging by temporal incident light modulation. *Optics Express*, 32 (11):18527–18538, 2024. 6

[31] Xinjie Yang, Qingmin Liao, Xiaowei Hu, Chenbo Shi, and Guijin Wang. Sepi-3d: soft epipolar 3d shape measurement with an event camera for multipath elimination. *Opt. Express*, 31(8):13328–13341, 2023. 1, 3

[32] Bohan Yu, Jieji Ren, Jin Han, Feishi Wang, Jinxiu Liang, and Boxin Shi. Eventps: Real-time photometric stereo using an event camera. In *Proceedings of the IEEE/CVF Conference on Computer Vision and Pattern Recognition*, pages 9602–9611, 2024. 1, 3

[33] Bohan Yu, Jinxiu Liang, Zhuofeng Wang, Bin Fan, Art Subpa-asa, Boxin Shi, and Imari Sato. Active hyperspectral imaging using an event camera. In *Proceedings of the Computer Vision and Pattern Recognition Conference*, pages 929–939, 2025. 1

[34] Xinyu Zhou, Peiqi Duan, Boyu Li, Chu Zhou, Chao Xu, and Boxin Shi. Evdig: Event-guided direct and global components separation. In *Proceedings of the IEEE/CVF Conference on Computer Vision and Pattern Recognition*, pages 9612–9621, 2024. 2, 3

Event-Based Multi-Range Radiance Separation and 3D Reconstruction via Line-Scan Pseudo-Square Illumination

Supplementary Material

6. Additional Results of Radiance Separation and Depth Estimation on Real Scenes

Figure 13 shows our radiance separation results of the monochrome setting. Three examples, "Carved bone," "Building blocks," and "Onigiri" are already shown in the main paper, but more enlarged images are provided here. Three additional examples "Soft toy," "Sandy-beach-like object," and "Shower puff" are newly provided. Appearance, estimated 2D depth map, and 3D visualization of the estimated depth of each scene are shown in Figure 11.

As a result of the "Soft toy" example, internal scatterings of the objects can be seen in 1- to 7-global images, and the interreflections of the scene can be seen in 15- and 21-global images. In the "Sandy-beach-like object" example, different intensity distributions are observed in each separated image depending on the material; interreflection makes the pebbles bright in 1- and 3- global images, and the frosted glasses are bright in 3- and farther global images due to subsurface scattering. Regarding the "Shower puff" example, direct component images reflect surface textures and surface specular reflections, while all the global images presents interreflection and scattering inside it.

Figure 14 shows our radiance separation results of the RGB setting. Three examples, "Anmitsu," "Flowers in a glass bowl," and "Pink flower" are already shown in the main paper, but more enlarged images are provided here. Three additional examples "Origami flower," "Plant and flowers," and "Yellow flower" are newly provided. Appearance, estimated 2D depth map, and 3D visualization of the estimated depth of each scene are shown in Figure 12.

Regarding the "Origami flower" example, structure-dependent differences in color distribution within the same flower are visualized by the separation of interreflected light. As for the "Plant and flowers" example, reflections on the surface of the wooden basket appear in direct image and interreflections in the intricate grass appear in long-range global. In the "Yellow-flower" example, the yellow color components of the flower can be dominantly seen in the direct image, and the global images reveal the flower's internal color.

All results of the separated r-global components and the estimated depth maps on each example are available in the supplementary video.

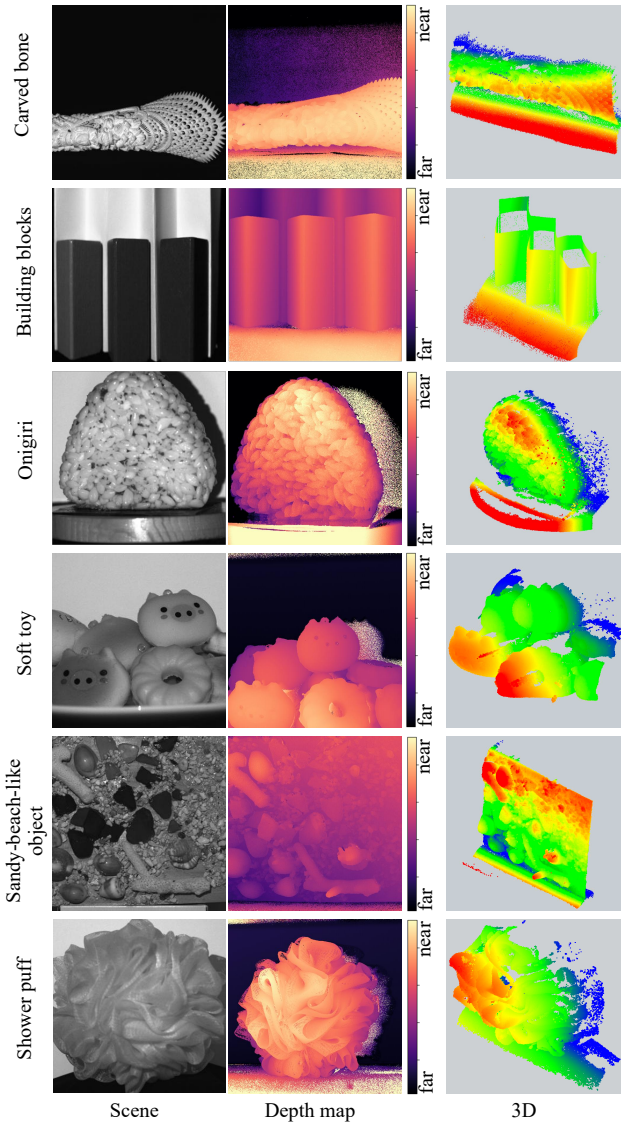

Figure 11. Appearance, estimated 2D depth map, and 3D visualization of estimated depth of scenes corresponding to Figure 13.

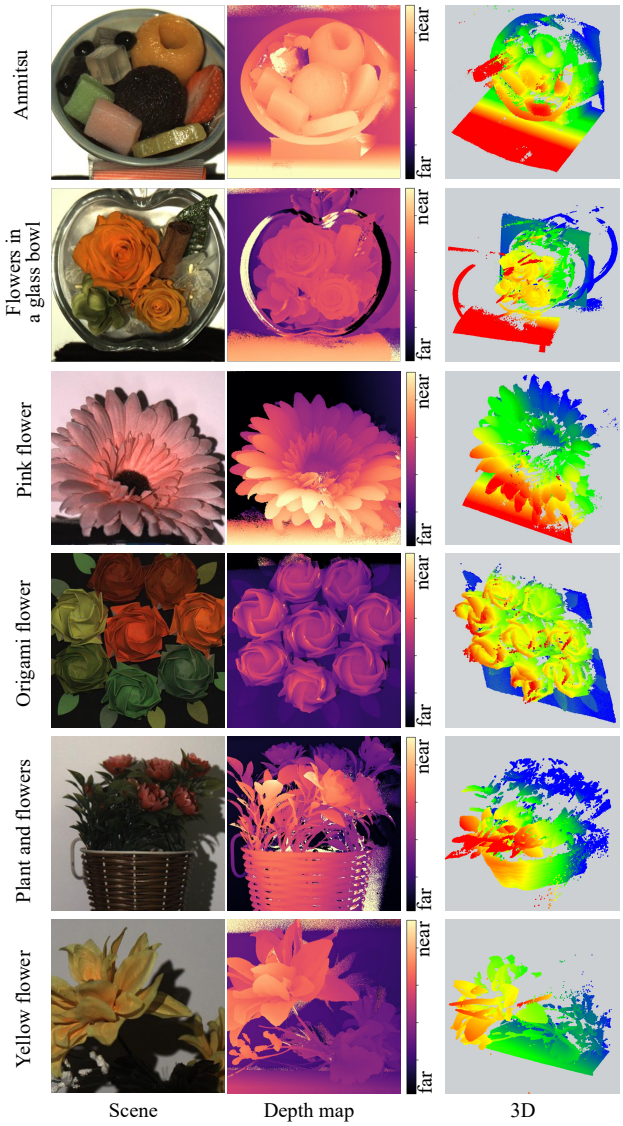

Figure 12. Appearance, estimated 2D depth map, and 3D visualization of estimated depth of scenes corresponding to Figure 14.

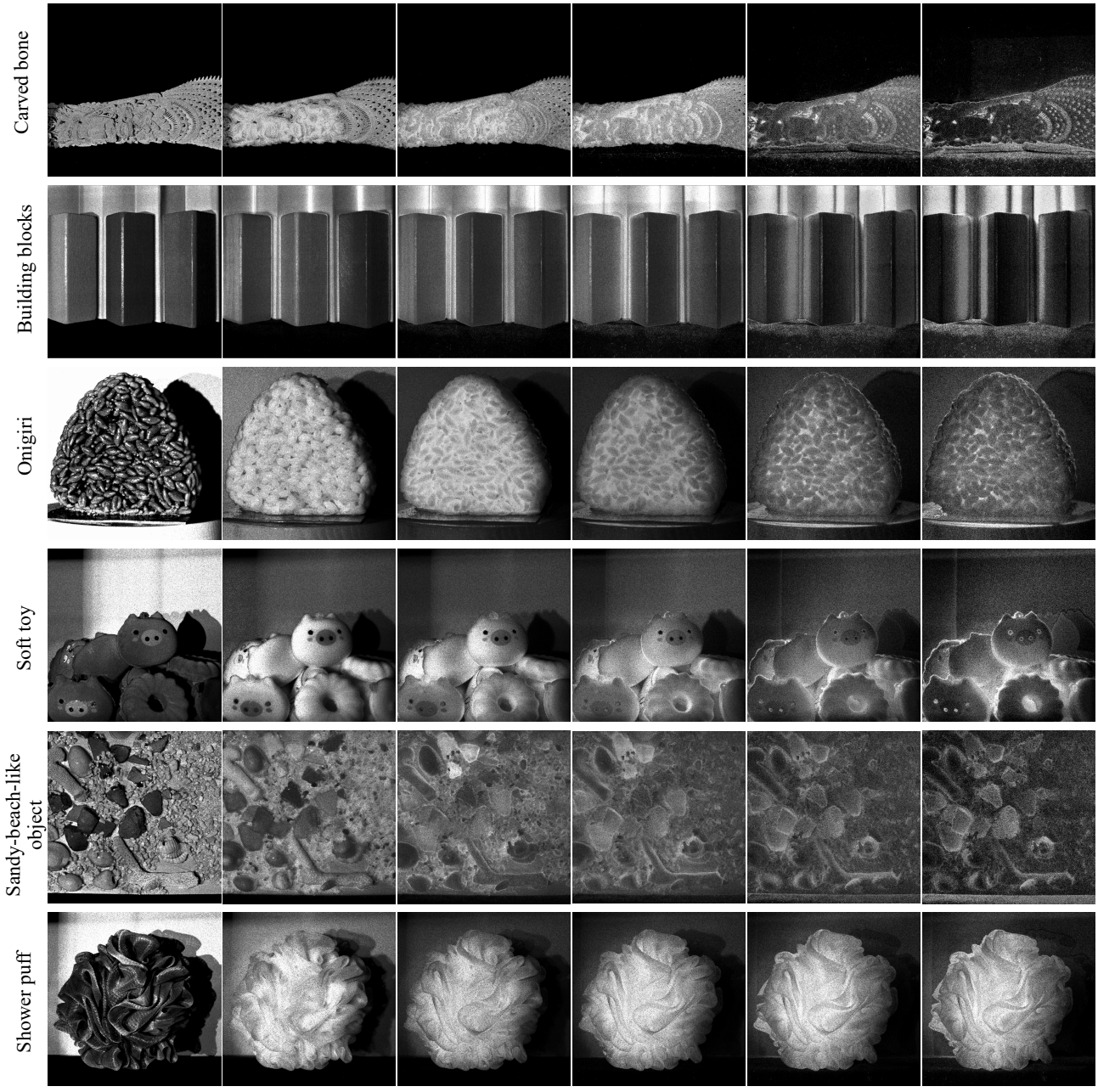

Figure 13. Radiance separation results of monochrome setting on real scenes. For each scene, the direct component and multiple r-global components are reconstructed from event-camera data. Note that the brightness of each component has been adjusted for visualization.

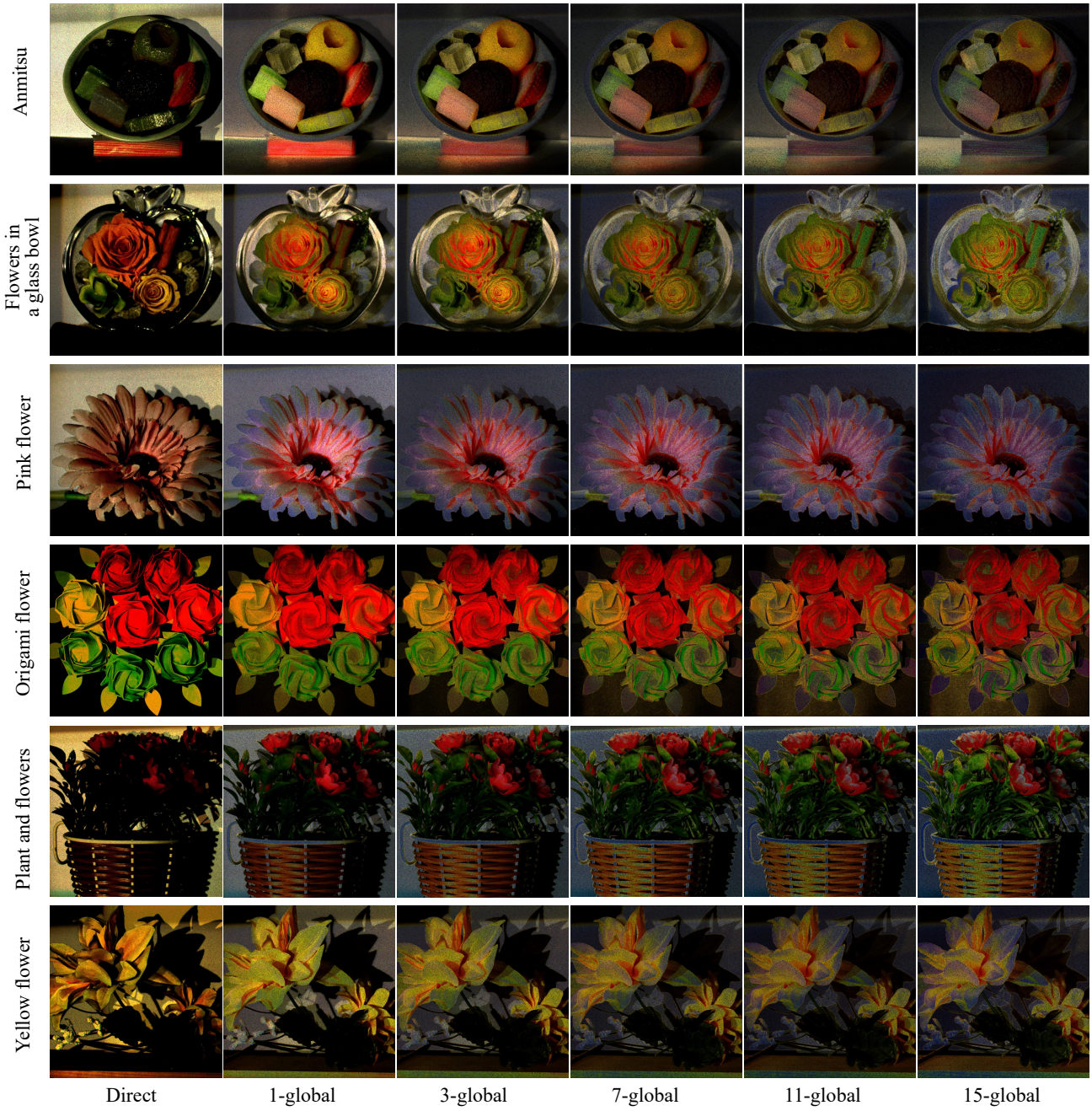

Figure 14. Radiance separation results of RGB setting on real scenes. For each scene, the direct component and multiple r-global components are reconstructed from event-camera data. Note that the brightness of each component has been adjusted for visualization.